ENVIRONMENTAL ENGINEERING SCIENCE
Volume 33, Number 1, 2016

DOI: 10.1089/ees.2015.0311

Characterization of Flocs and Floc Size Distributions Using Image Analysis

Siwei Sun, Monroe Weber-Shirk,** and Leonard W. Lion*

School of Civil and Environmental Engineering, Cornell University, Ithaca, New York.

Received: August 19, 2015 *Accepted in revised form: October 15, 2015*

Abstract

A nonintrusive digital imaging process was developed to study particle size distributions created through flocculation and sedimentation. Quantification of particle size distributions under different operating conditions can be of use in the understanding of aggregation mechanisms. This process was calibrated by measuring standardized polystyrene particles of known size and was utilized to count and measure individual kaolin clay particles as well as aggregates formed by coagulation with polyaluminum chloride and flocculation. Identification of out-of-focus flocs was automated with LabVIEW and used to remove them from the database that was analyzed. The particle diameter of the test suspension of kaolinite clay was measured to be $7.7 \pm 3.8\,\mu$m and a linear relationship was obtained between turbidity and the concentration of clay particles determined by imaging. The analysis technique was applied to characterize flocs and floc particle size distribution as a function of coagulant dose. Removal of flocs by sedimentation was characterized by imaging, and the negative logarithm of the fraction of turbidity remaining after settling had a linear relationship with the logarithm of aluminum dose. The maximum floc size observed in the settled water was less than $120\,\mu$m, which was in accordance with the value predicted by a model for the capture velocity of the experimental tube settler of 0.21 mm/s.

Key words: capture velocity; flocculation; floc size distributions; image analysis; particle size measurement; tube settler

Introduction

Flocculation facilitates aggregation of inorganic and organic colloids in water sources and is a crucial pretreatment process before particle removal by sedimentation and filtration. The fluid velocity gradient (G) is widely recognized as a key design parameter for laminar flow flocculators. Many studies have shown a relationship between floc sizes and G (Matsuo and Unno, 1981; Hopkins and Ducoste, 2003). The energy dissipation rate (ε) is also used in the design of water treatment plants and, under conditions of laminar flow, is related to the average velocity gradient $\overline{G}$ as follows (Coufort *et al.*, 2008):

$$\overline{G} = \sqrt{\frac{\varepsilon}{v}} \tag{1}$$

where ε is the average energy dissipation rate and v is the kinematic viscosity of fluid.

Terminal velocity is the settling velocity of a floc when the forces of gravity and drag plus buoyancy are equal. Flocs are very likely to be captured by settling if their terminal velocity is higher than the capture velocity of the settling tube. The terminal settling velocity for flocs was defined by Adachi and Tanaka (1997) as follows:

$$v_t = \frac{g d_{clay}^2}{18 \Phi v_{H_2O}} \frac{\rho_{clay} - \rho_{H_2O}}{\rho_{H_2O}} \left(\frac{d}{d_{clay}}\right)^{D_{fractal}-1} \tag{2}$$

where Φ is the shape factor for drag on flocs, d is the diameter of floc, v_{H_2O} is the kinematic viscosity of water, ρ_{clay} is the density of primary clay particles, ρ_{H_2O} is the density of water, d_{clay} is the diameter of the primary particles, d is the floc diameter, and $D_{fractal}$ is the 3D fractal dimension of flocs. The shape factor accounts for the adjustment of the coefficient of drag for nonspherical geometry and has a value of 45/24 (Adelman *et al.*, 2013).

Li and Ganczarczyk (1989) calculated the fractal dimensions of the alum aggregates based on the reported data of settling tests and size–density relationships. The fractal dimension from Boadway's (1978) data is calculated to be around 2.3 and the one from Tambo and Watanabe (1979) is between 1.59–1.97.

In the experimental tube settler, the particle removal efficiency can be quantified by pC*, which is defined by the following equation:

$$pC^* = -\log_{10}\left(\frac{C_{effluent}}{C_{influent}}\right) \tag{3}$$

*Member of AEESP.
**Corresponding author:* School of Civil and Environmental Engineering, Cornell University, 265 Hollister Hall, Ithaca, NY 14853. *Phone:* (+1) 607-216-8445; *Fax:* (+1) 607-255-9004; *E-mail:* mw24@cornell.edu

where $C_{effluent}$ is the effluent turbidity and $C_{influent}$ is the influent turbidity.

During flocculation, particle sizes, structures, and shapes can all affect the aggregation behavior and collision efficiency (Jiang and Logan, 1991). Yao *et al.* (2014) reported that concentration of particles less than 5 μm is proportional to water turbidity in the range of 0–40 nephelometric turbidity units (NTUs). Nan *et al.* (2009) suggested that flocs in different size ranges contribute differently to the decrease in turbidity after sedimentation. Some of the fundamental mechanisms that control flocculation are still not well understood. For instance, Swetland *et al.* (2014) observed that small particles do not readily attach to big flocs so that aggregation occurs slowly. There appears to be something about the collisions between particles that are very different in size that makes aggregation difficult. The development of an analytical tool to nondestructively characterize temporally evolving flocculent particle size distributions can lay a foundation for studies of particle collisions and the mechanisms that control aggregation. Understanding how floc size distribution influences the flocculation process will, in turn, contribute to the optimization of water treatment plant design.

Particle size characterization can be accomplished using a Coulter counter (Zhang *et al.*, 2007) or by the electrical sensing zone method (Gibbs, 1982). However, both analyses require withdrawal of samples from a suspension that may disrupt fragile flocs (Chakraborti *et al.*, 2000). Some researchers have adopted photographic techniques and image analysis as noninvasive tools for the continuous measurement of changes in floc sizes in jar tests. Bouyer *et al.* (2004) used a laser beam as light source and VISILOG 5 for image analysis to obtain the instantaneous size distribution of flocs. However, they found it difficult to exploit the data without analyzing the contour of particles because there were too many possible intersections between the laser plane and particle shapes, and particle data needed to be discarded if the contour of the particle was shaded. Particle image velocimetry software for image acquisition and storage and NIH Image software for image analysis have been used by Chakraborti *et al.* (2000) to characterize alum flocs. Keyvani and Strom (2013) developed a fully automated image processing script to remove out-of-focus particles to attain more precise size distributions with ImageJ and MATLAB.

The goal of this research was to develop a fully automated tool for image analysis of flocculent particle suspensions. Necessary tool characteristics were the ability to identify out-of-focus images to exclude them from the data set and to obtain accurate particle characteristics suitable for calculation of particle size distributions. Based on Keyvani and Strom's study, an image analysis script was developed in this research using the National Instruments LabVIEW and Vision Builder Toolkit to explore particle size distribution changes during flocculation and sedimentation. The LabVIEW software incorporates image acquisition and analysis.

Experimental Methods

Flocculator setup

Figure 1 shows a schematic of the laboratory apparatus. Aerated Cornell University tap water was pumped from a temperature-controlled reservoir and mixed with a concentrated kaolinite (R.T. Vanderbilt Co., Inc.) clay stock to form synthetic raw water. Raw water turbidity was controlled by adjusting the flow rate of clay stock and was continuously measured using a MicroTOL 3 turbidity meter (Model number: 20055; HF Scientific, Inc.). The turbidity meter was equipped with a flow cell so that there was no need to withdraw samples from the raw water. Polyaluminum chloride (PACl) coagulant doses (Holland Company) ranging from 0.53 to 2.65 mg/L as Al were mixed into the raw water. Flocculation was accomplished by laminar flow through a coiled 9.52-mm (inner diameter) tube. Flow rate inside the flocculator was 3.6 mL/s, and the hydraulic residence time was 300 s. Sedimentation occurred in a 1.37 m tube settler (whose inner cross-sectional dimensions were 2.22×2.22 cm and angle of inclination was 60°) with a capture velocity (also

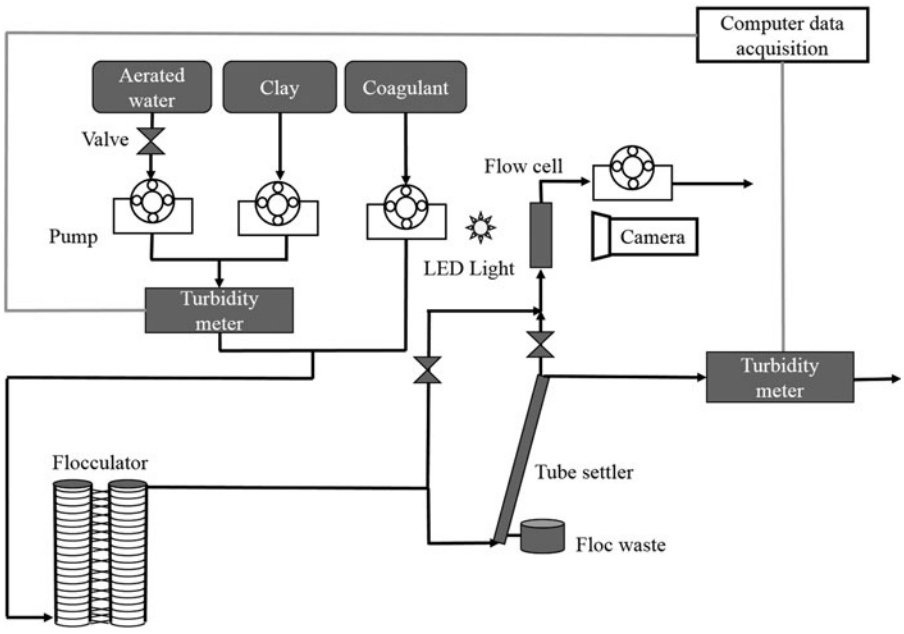

FIG. 1. Schematic of experimental apparatus.

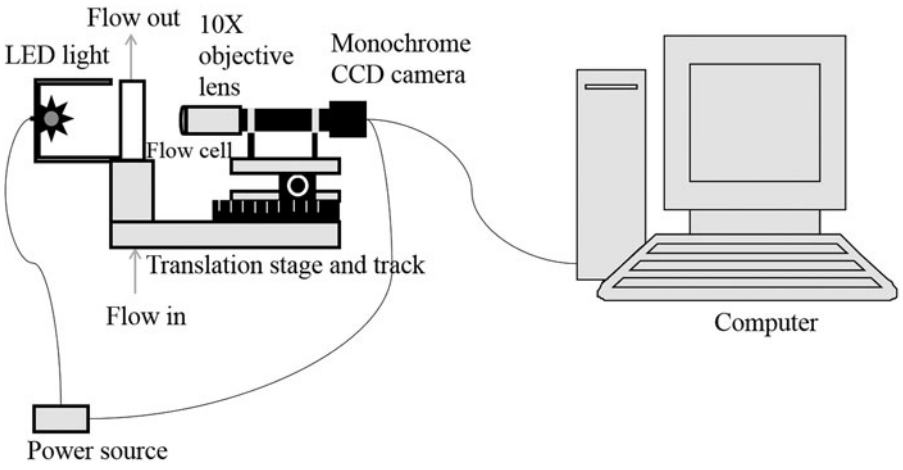

FIG. 2. Imaging system consisting of an LED light, CCD camera attached to a computer, and suspended sample in a flow cell.

referred to as a critical velocity) of 0.21 mm/s. Approximately 8% of the experimental flow could be directed to a flow cell. Two ball valves were utilized to control the type of water entering the flow cell, allowing imaging of either flocculated water or settled water. Effluent turbidity was continuously measured using a MicroTOL 2 turbidity meter (Model number: 20053; HF Scientific, Inc). Process Controller software created using LabVIEW by Weber-Shirk (2008) was utilized for acquisition of turbidity data.

In laminar flow, there is no turbulence to resuspend particles that may settle in the flocculator. As a result, the experimental flocculator tubing was coiled in a figure-eight configuration to create a secondary flow circulation to prevent floc sedimentation (Tse *et al.*, 2011).

The average velocity gradient ($\overline{G}_c$) in the coiled figure-eight flocculator that accounts for the secondary flow was calculated as described by Tse *et al.* (2011):

$$\overline{G}_c = \overline{G}\sqrt{1+0.033\left[log\left(\frac{4Q_{plant}}{\pi Dv}\sqrt{\frac{D}{R_c}}\right)\right]^4} \qquad (4)$$

where Q_{plant} is the experimental flow rate, D is the inner diameter of the flocculator tube, and R_c is the diameter of curvature of the flocculator coils (0.22 m).

The average energy dissipation rate of the flocculator was 5 mW/kg and the average velocity gradient was calculated to be 70.6/s (see supplementary information).

Imaging system

The camera system (Fig. 2) consisted of an LED light source and Flea3 FL3-GE-13S2M monochrome GigE camera (Point Grey Research, Inc.) controlled by the LabVIEW program. The camera was a 1288×964 pixel progressive scan, monochrome 1/3'' CCD fitted with an M Plan Apo 10× infinity-corrected objective lens with a numerical aperture of 0.28 (Mitutoyo Corporation). The camera can capture continuous images at up to 31 frames/s or single images by external trigger or through software control.

Based on the camera sensor format and 10× magnification of the objective lens, the field of view for the imaging system was 480×360 μm. Each pixel sampled an area in the field of view of 0.375 by 0.375 μm. The depth of field of the objective lens was calculated over a range of influent turbidities and the average value was 500 ± 90 μm [Eq. (10)]. The constraints for maximum floc size measurements are the field of view and the depth of field of the lens. For flocs smaller than this depth of field, it is likely that the entire floc will be in focus.

The diffraction of visible light (~400–700 nm) (Pal and Pal, 2001) can result in airy disks around particles in images and error in particle size measurements. An airy disk is a bright central core surrounded by diffraction rings. More than 80% of light energy concentrates in the central ring of the airy disk (Greivenkamp, 2004), as shown in the intensity distribution in Fig. 3A.

A consequence of the formation of airy disks is that a point in an object will not be imaged as a spot with sharply defined

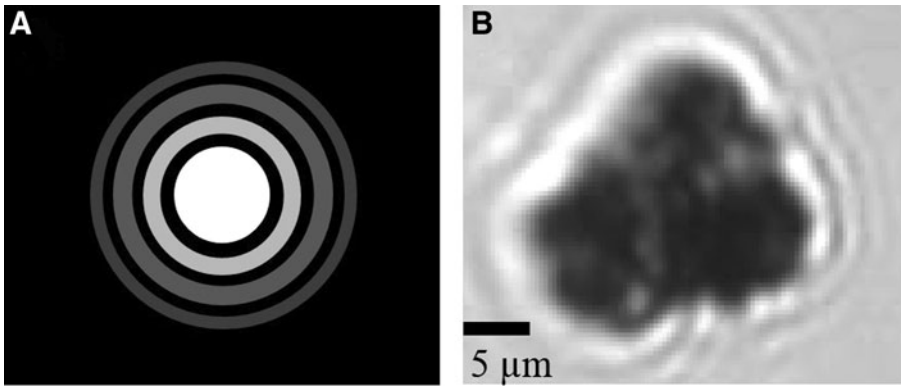

FIG. 3. Airy disks. **(A)** Airy pattern and intensity distribution. **(B)** Airy patterns around a particle.

edges. Instead, it is imaged by the objective lens as a spot surrounded by diffraction rings, which can affect the accuracy in measuring particle diameters. Figure 3B illustrates one example showing the airy patterns around a particle. It is obvious that the edges of the floc are not sharply contrasted.

The radius of the central ring of the airy disk can be calculated (Edmund Optics, 2015) as follows:

$$r_{airy\ disk} = \frac{0.61\lambda}{NA} \tag{5}$$

where λ is the wavelength of the incident light and *NA* is the numerical aperture, which was ~ 0.28 for the objective lens used in this research.

The estimated radius of airy disk caused by yellow light ($\lambda \approx 590nm$) is around 1.29 μm. Since each point around the particle has an airy pattern, particles less than $1.29 \times 2 \approx 2.6$ μm in diameter (particle area of $\sim$39 pixels) cannot be clearly identified. The apparatus could thus measure particle sizes ranging from 2.6 μm (set by the airy disk) to more than 300 μm (set by the field of view). Standardized particles of known size were utilized to determine the error in particle size measurement caused by light diffraction.

The camera was connected to the computer through Gigabit Ethernet, which allowed an acceptable transfer speed of 100 MB/s (equivalent to 2,226 images of JPEG format/s). The camera was mounted on a horizontal translation stage fixed to an aluminum platform. An LED light provided bright-field illumination of flocs in the flow cell (Keyvani and Strom, 2013).

The flow cell was constructed from a glass cuvette with a cross-sectional area of 1×1 cm. The inlet and outlet of the flow cell had a diameter of 7.1 mm. The flow rate inside the flow cell was constrained by the minimum shutter speed of the digital camera. It was assumed that blurry images could occur when a pixel moved 1/4 of its length. Therefore, the maximum flow rate inside the flow cell was calculated by Equation (6).

$$Q_{flowcell} = 0.375\ \mu m \times \frac{1}{4} \times \frac{A_{flowcell}}{t} \tag{6}$$

where $A_{flowcell}$ is the cross-sectional area of the flow cell and t is the time the shutter is open (33 μs).

Flow rate through the sample cell was set to 0.28 mL/s based on Equation (6). The average velocity gradient in the inlet port of the flow cell was 5.4/s, making the average velocity gradient entering the flow cell less than 7.6% of the average velocity gradient in the flocculator. The average velocity of the water flowing through the flow cell was 2.84 mm/s. This velocity was also much higher than the sedimentation velocity (0.72 mm/s) of the largest flocs (around 300 μm) the camera can measure. Floc images were taken every 1 s by the camera so that the same particle would not be imaged more than once.

During initial testing of the imaging system, the optimal shutter speed for image contrast was determined to be 330 μs or 10 times longer than the minimum shutter speed. The particle travel distance during this time is 1 μm and there was no evidence of significant image blurring. The 1 μm travel distance during the time when the shutter is open is small compared with the minimum particle size of 2.6 μm.

Image analysis

The image analysis script accomplished four functions: (1) reduction of image noise, (2) identification of particles from background, (3) removal of particles that were out of focus or that had portions beyond the image border, and (4) calculation and recording of particle sizes. The image processing functions prepackaged in LabVIEW are capable of identifying and measuring particles. These functions include filters, threshold, basic or advanced morphology, and particle analysis (National Instruments, 2008).

Identification of particles

A filter was first applied to each image to reduce small changes in pixel values caused by variability in the charge-coupled device of the camera. The Gaussian filtering function of the LabVIEW vision application was found to work best at reducing noise by attenuating the variations of gray scale intensity in a pixel's neighborhood. The Gaussian filter effectively smoothed the fuzzy edge of the particles in the image so that one could better extract useful information from a particular image.

Filtering was followed by the operation of thresholding, which distinguished particles from the background and produced a binary image with 0 representing the background and 1 representing particles. In general, there are two thresholding methods: global thresholding and local thresholding. Global thresholding identifies particles based on a single gray scale value. In local thresholding, each pixel is categorized based on the intensity of pixels in its neighborhood (National Instruments, 2013). Global thresholding usually requires a specified threshold range for each set of tests, while local thresholding can identify particles automatically. Thus, background correction (National Instruments, 2013) within the local thresholding function was utilized in the image

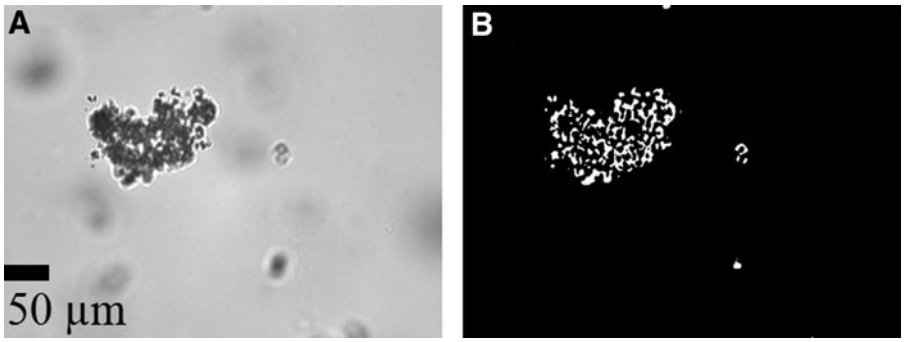

FIG. 4. Application of local thresholding. **(A)** Original image with flocs. **(B)** Local thresholding applied to image **(A)**.

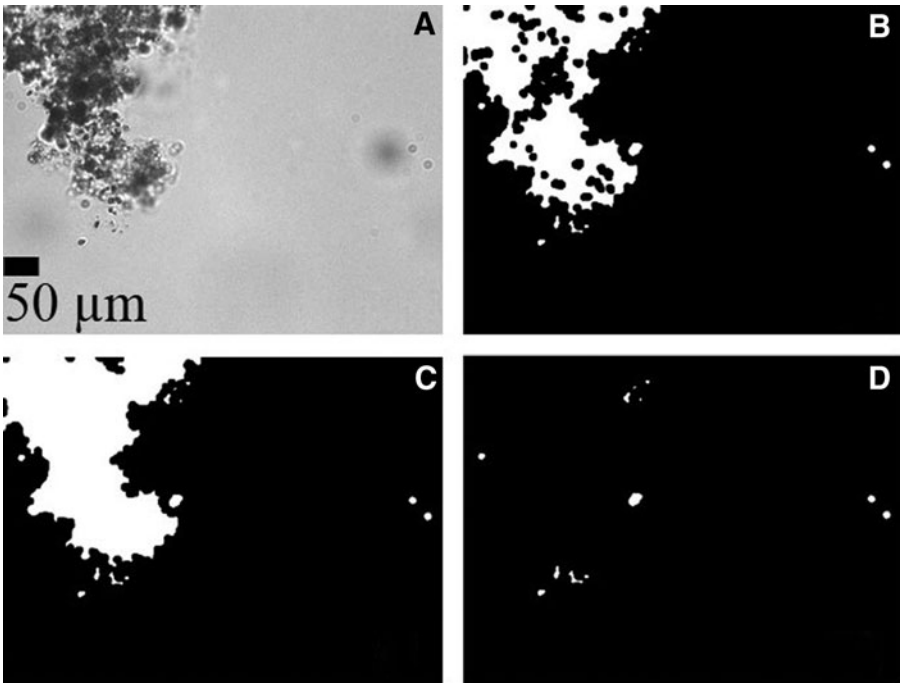

FIG. 5. Example of morphological transformation. **(A)** Original gray scale image, **(B)** image after background correction and closing objects, **(C)** image after filling holes, **(D)** image after removing small particles or particles that touched the border of the image.

analysis procedure in this research, in that this technique is well suited for conditions where images exhibit nonuniform light intensities caused by other out-of-focus particles in the background.

Figure 4 shows the application of local thresholding (background correction). This local thresholding method appears to function well in particle recognition.

When local thresholding is applied to an image, holes and gaps inside a floc can arise due to the complicated structure of the aggregates. The holes and gaps must be filled to calculate the particle area. Thus, some morphological transformations were utilized to prepare particle images for quantitative analysis. These transformations included closing the object perimeter, filling holes, and removing particles touching the border, as well as small particles less than 39 pixels (equivalent spherical diameter of 2.6 μm). Particles less than 39 pixels were not considered because they were too small to obtain an accurate measurement of their shape and area as a result of airy disk patterns.

The closing objects function was able to fill small holes and smooth out the boundaries of the floc. These changes only slightly alter the shape or the area of the object. The filling holes function filled any remaining holes inside the particle boundary. Figure 5 shows an example of the morphology transformation functions.

The next step in image analysis was to measure the area and the coordinates of the bounding rectangle of each floc in pixels. The spherical equivalent diameter in pixels can be calculated as follows:

$$d_{pixel} = \sqrt{\frac{4A_{pixel}}{\pi}} \tag{7}$$

where A_{pixel} is the projected area of the particle, in pixels. As mentioned above, particle sizes were also corrected in this step to account for the influence of airy disks.

The region of interest (ROI) for each floc was defined by the coordinates of the bounding rectangle. The floc ROI of the original image was used to assess if the floc was in focus.

Removing out-of-focus particles

As noted above, local thresholding could identify almost all particles within an image regardless of their degrees of focus, except for some extremely blurry flocs, such as the ones in Fig. 4A. Hence, the next part of the image analysis script acted to remove out-of-focus flocs.

Whether an object in an image appears blurry or not is determined by its focus quality characterized by the sharp differences between background and object edges (Klinger, 2003). Keyvani and Strom (2013) introduced a concept of clarity value index to determine the focus quality of each floc and thus distinguish in-focus particles from the blurry ones. In their work, each image was treated with a convolution of a first Gaussian kernel in both horizontal and vertical directions. The maximum value of the filtered image associated with each floc could be used to define how close the floc was to the focal plane.

Flocs that are in focus have sharp gradients between the background and the floc. Flocs that are out of focus have weaker gradients at their boundaries. The image gradient intensity at the floc boundaries was used to eliminate flocs that were not in focus. A sobel filter works as an edge detector and computes an approximation of the image intensity gradient by convolving the image with a filter in both horizontal and vertical directions. High sobel filter values indicated the floc was in focus. The maximum image intensity gradient was computed for each floc. To eliminate the effect of LED light intensity and shutter speed (which will have influence on the light intensity), the maximum image intensity gradient was divided by the mean pixel value of the whole image. The

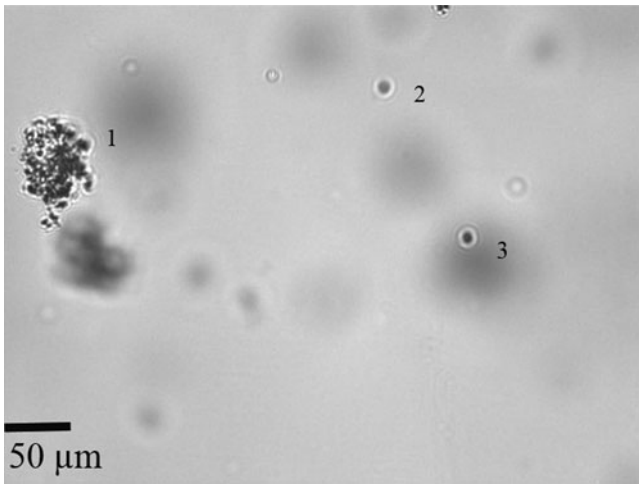

FIG. 6. Sample image of identified and measured flocs. Numbered flocs and particles are those referred to in Table 1.

result was then multiplied by a length scale ($3 \times 0.375\ \mu$m) related to kernel size (a kernel is a 3×3 matrix for a sobel filter) to give in a dimensionless parameter used to discriminate between in-focus and out-of-focus flocs.

$$\alpha = \frac{\min\left[I(ROI_i)\right]}{mean[I(ROI_i)]} \tag{8}$$

$$\beta = \frac{\max\left[I_f(ROI_i)\right] \times l}{mean[I(ROI_i)]} \tag{9}$$

where α is the normalized minimum pixel value, I is the matrix of the original image pixel values, ROI_i is the bounding rectangle of floc i, β is the dimensionless maximum floc image intensity gradient, I_f is the sobel filter of the image matrix, and l is the length scale of the sobel filter kernel, which is 1.1 μm.

Darker flocs (which have smaller pixel values) were closer to the focal plane. Thus, the minimum pixel value (α) of I (the original image matrix) associated with each floc was also measured to assist in the determination of focus quality. Some transparent particles of unknown origin were observed in the clay mixture with a β greater than 0.16. These unknown particles were discarded by setting a minimum pixel value of I. The minimum pixel value of the original image was normalized to be dimensionless as described above.

Threshold values for both α and β were used to distinguish in-focus particles from those which were not in focus and were determined by examining computed values from a great number of images. After comparison, the image intensity gradient threshold value (β_t) was set to be 0.16 and the threshold value of the normalized minimum pixel value (α_t) to be 0.56. Therefore, particles with β above 0.16 and α below 0.56 were considered as in-focus flocs and the remaining flocs were removed from the database. The calculated spherical equivalent diameters of those in-focus flocs were then written to a cvs file for each image.

Figure 6 is one example showing different α and β values and the focus quality within an image. In Fig. 6, three flocs are identified after thresholding (actually four particles were identified; however, one touching the top border was removed). Floc 1 has the best focus quality; flocs 2 and 3 may possibly be in focus. As is shown in Table 1, a value of $\beta_t = 0.16$ and a value of $\alpha_t = 0.56$ worked well as a particle

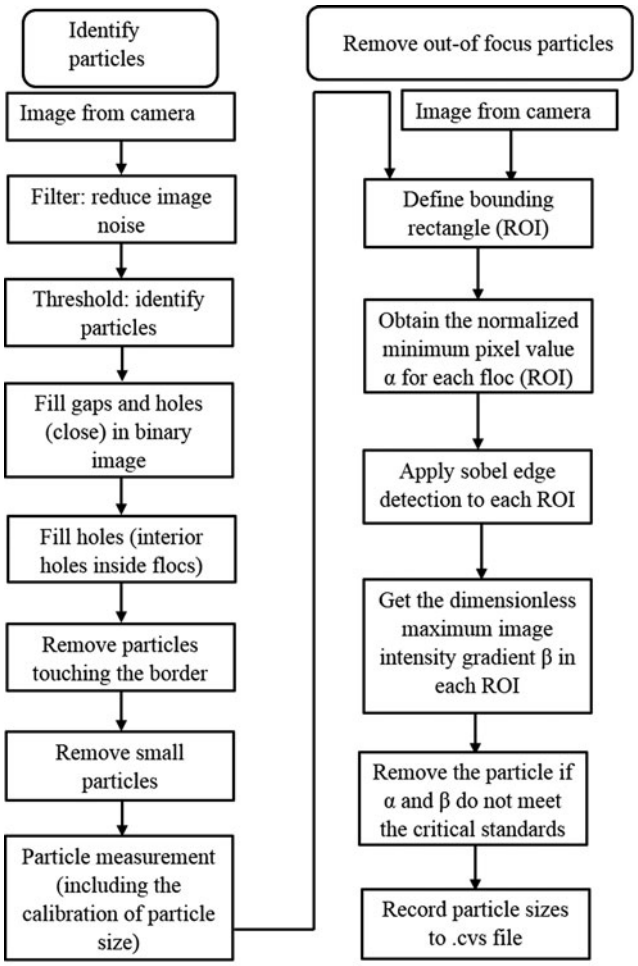

FIG. 7. Flowchart of image analysis procedure.

TABLE 1. IDENTIFIED FLOCS IN FIGURE 6 WITH ASSOCIATED α AND β VALUES

Floc number	α	β	*Acceptable*	*Spherical diameter (μm)*
1	**0.26**	**0.69**	**Yes**	56.4
2	0.65	0.15	No	—
3	**0.37**	**0.20**	**Yes**	6.9

Bold values meet the constraints.

TABLE 2. MEAN AND STANDARD DEVIATION FOR 3.0 μM STANDARDIZED PARTICLES

3.0 μm particles	*Coulter multisizer (μm)*	*Image analysis (μm)*
Mean	2.83	5.45
Standard deviation	0.07	1.09

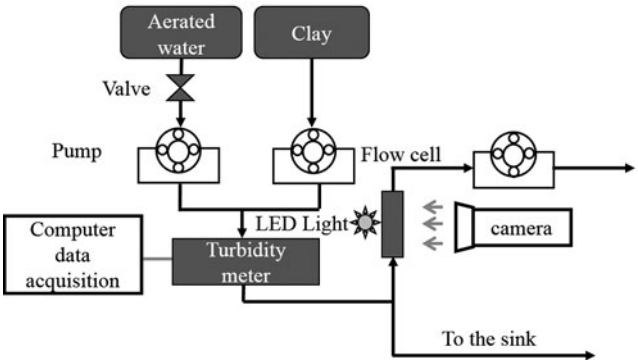

FIG. 8. Schematic of experimental setup for image analysis method verification.

filter, removing the out-of-focus flocs and retaining the in-focus ones.

Figure 7 summarizes the order of operations performed on each image to obtain the geometric characteristics of particles.

Results

Validation of image analysis method

Sizes of standardized particles were tested to determine the error caused by light diffraction in the camera setup. More than 300 images of the suspensions of dark blue polystyrene particles with nominal size of 3.0 μm (Sigma-Aldrich) were captured. The images were then processed using the image analysis tool. The manufacturer determined the diameter of the standardized microparticles using a Coulter multisizer II. As is shown in Table 2, the average particle size measured by the image system was greater than the values obtained by the manufacturer by 2.6 μm, which was consistent with the estimated diameter of the airy disk.

The image analysis method was then used to measure the diameter of clay particles at different turbidities in the absence of coagulant, with the apparatus configured as shown in Fig. 8. Based on the calibration, a correction of 2.6 μm was subtracted from the mean diameter measured by the image analysis software.

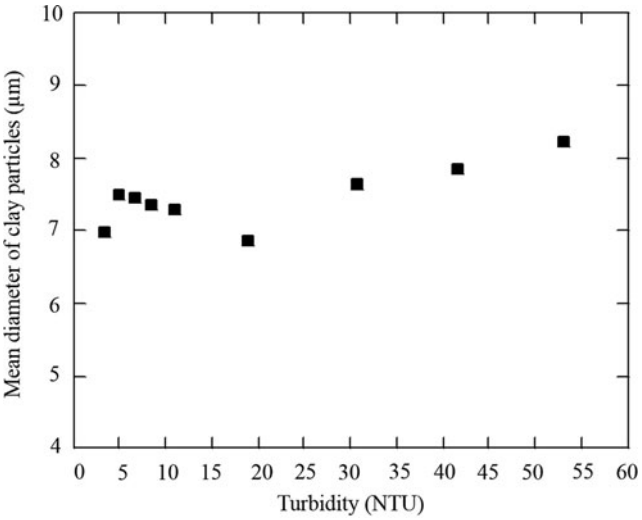

FIG. 9. Average diameter of clay particles at different turbidities.

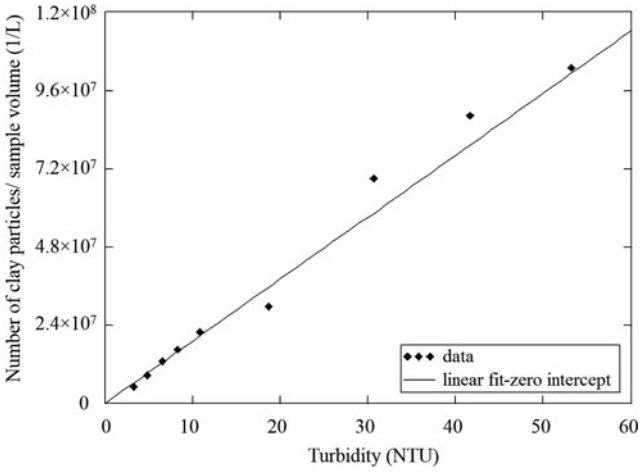

FIG. 10. Number of clay particles per sample volume versus turbidity.

Kaolinite particles have a reported diameter ranging from 0.2 to 12 μm (Aroke *et al.*, 2013). The mean volume diameter of a 100 mg/L kaolinite suspension (the turbidity was 68 NTUs) was measured by a Mastersizer 2000 as 7.28 μm (Wei *et al.*, 2015). The average measured diameter of the test clay particles was 7.7 ± 3.8 μm after correction for the airy disk, which was within the reported size range for kaolinite and was quite close to the mean diameter of 7.28 μm measured by Wei *et al.* (2015). Figure 9 illustrates the average measured clay diameters at different turbidities.

The depth of field of the lens is not specified by the manufacturer, but it can be estimated. The depth of field is expected to be a function of the β_{Min} value used to identify which flocs are sufficiently in focus for further analysis.

The depth of field, H_{image}, could be derived from the following equation:

$$H_{image} = \frac{V_{clay} \cdot \rho_{clay}}{1.73 \frac{mg}{L \cdot NTU} Turbidity \cdot W_{image} \cdot L_{image}} \quad (10)$$

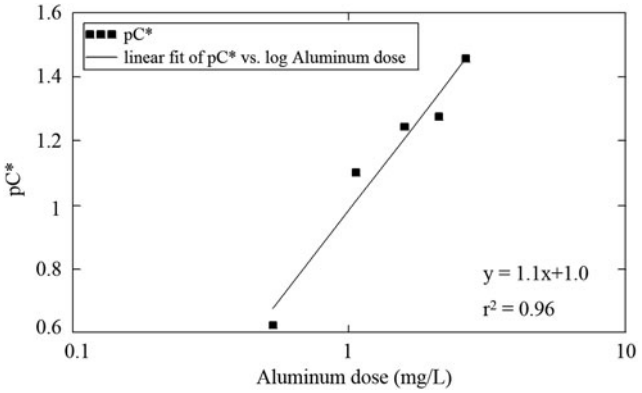

FIG. 11. pC* versus polyaluminum chloride (PACl) dose (mg/L as Al).

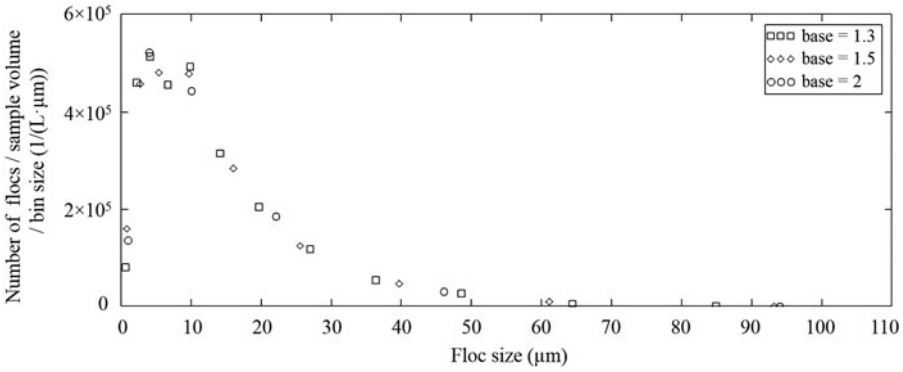

FIG. 12. Floc size distributions of settled water according to different bin sizes (PACl dose = 0.53 mg/L as Al).

where W_{image} is the width of the image, L_{image} is the height of the image, V_{clay} is clay volume measured in one image based on the assumption that the clay particles were spheres, ρ_{clay} is clay density and has a value of 2.5 g/cm^3, and 1.73 $\frac{mg}{L \cdot NTU}$ was measured in the Cornell Environmental Engineering laboratory by Casey Garland (pers. comm., June 13, 2015). This is similar to the value of 1.5 $\frac{mg}{L \cdot NTU}$ obtained by Wei *et al.* (2015).

Depth of field was calculated to be 500 ± 90 μm for a range of influent turbidities. For flocs smaller than this depth of field, it is likely that the entire floc will be in focus.

Figure 10 shows that there was a linear relationship between turbidity and the number concentration of clay particles based on the depth of field calculated previously.

A linear fit with a zero intercept was obtained by calculating the average slope between each data point and the origin. The slope of the linear fit was 1.9E6 $\pm$ 2.2E5 $\frac{1}{L \cdot NTU}$. Thus, there were 1.9 million clay particles per $L \cdot NTU$. An $L \cdot NTU$ is equivalent to 1.73 mg of clay and, given the density of clay, is equivalent to a clay volume of 0.68 μL. Thus, the average volume of the clay particles was 360 μm^3, which yields an equivalent diameter of 8.8 μm. This is the volume-weighted average diameter of the clay particles and thus gives a slightly larger diameter than the count-weighted average diameter of 7.7 ± 3.8 μm.

Effect of coagulant dose

Image analysis was performed on settled water to obtain floc number concentration and size distributions, along with measurement of effluent turbidity.

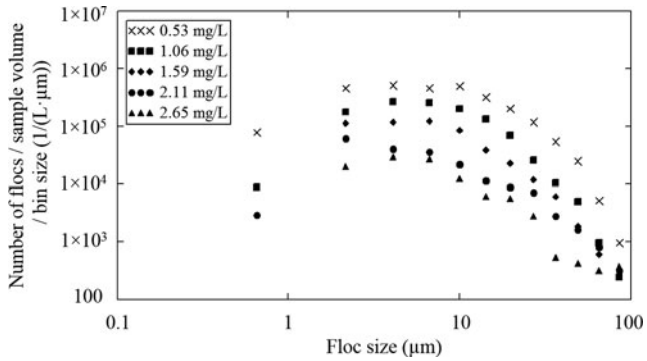

FIG. 13. Floc size distributions of settled water at different PACl doses (mg/L as Al).

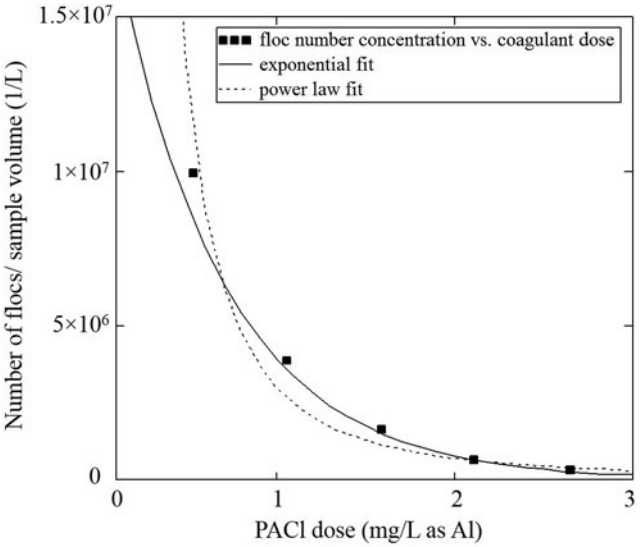

FIG. 14. Floc number concentration in settled water versus PACl dose (mg/L as Al).

Figure 11 shows pC* values over a range of PACl doses; a pC* value of 1 indicates 90% removal efficiency, a pC* of 2 indicates 99%, and so on. The aluminum doses applied to 50 NTUs raw water were 0.53, 1.06, 1.59, 2.11, and 2.65 mg/L. As is shown in Fig. 11, pC* increased when PACl dose increased and there was a linear relationship between pC* and the logarithm of PACl dose.

The result in Fig. 11 agrees with the flocculation model created by Swetland *et al.* (2014). These investigators observed a linear relationship between pC* and the logarithm of colloid surface coverage by coagulant (which is proportional to coagulant dose at low doses). The slope in Fig. 11 was 1.1 and is close to the slope of 1 for the model indicated by Swetland *et al.* (2014).

TABLE 3. EXPONENTIAL FIT AND POWER LAW FIT IN FIGURE 14

Trend line option	*Trend line equation*	r^2
Exponential fit	$y = 2 \times 10^7 e^{-1.6x} \frac{1}{L}$	1.00
Power law fit	$y = 3 \times 10^6 x^{-2.1} \frac{1}{L}$	0.96

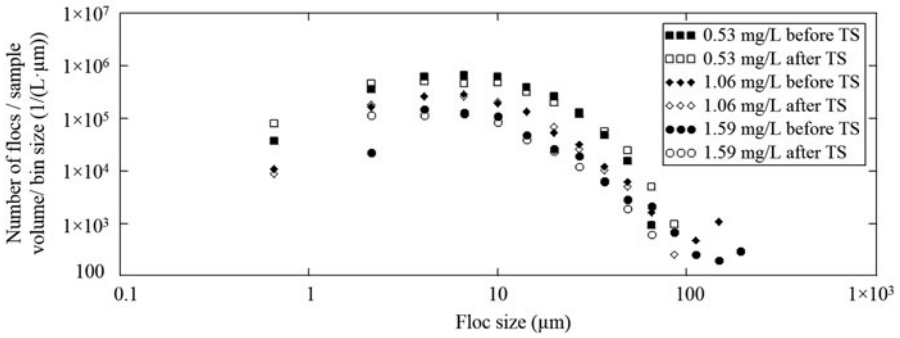

FIG. 15. Size distributions of flocculated water and settled water at different PACl doses (mg/L as Al). TS designates tube settler.

Figure 12 illustrates the distribution of floc number concentration allocated to different bin sizes. The horizontal axis in Fig. 12 is the spherical equivalent floc diameter, while the vertical axis is the total number of flocs per sample volume per bin size within each floc size range. For each set of data, the bin size was varied in a power law relationship to a base. For instance, when the base is selected to be 1.3, the size of the first bin would be 1.3 μm and the first bin is defined by a lower bound of 0 μm and an upper bound of 1.3 μm, the second bin size is 1.3^2 μm (= 1.7 μm) and the lower and upper bounds are 1.3 and 3.0 μm, the third bin is 1.3^3 μm (= 2.2 μm) and its lower and upper bounds are 3.0 and 5.2 μm, and so on. The median value of each bin is considered as the mean diameter of flocs for that size range. The number of flocs within each bin was then counted by the LabVIEW histogram function.

For alternative bases, there were only slight changes in the shape of the distribution curve and the area under the curve. This result indicates that the specification of bin size over the range tested had little impact on the particle size distribution curve.

Figure 13 indicates that the number concentration of flocs in the settled water decreased with the increase in PACl dose. According to Equation (2), flocs larger than 120 μm have a terminal velocity greater than capture velocity of tube settler of 0.21 mm/s (based on a fractal dimension of 2.3), which means the removal efficiency of those flocs is expected to be 100%. As seen in Fig. 13, the maximum floc size observed in the settled water was less than 120 μm, which is in agreement with the model.

Figure 14 suggests that the number concentration of flocs in the settled water decreases as a function of coagulant dose. Both an exponential and power law provided a good fit to the data in Fig. 14. The fits to the data are shown in Table 3.

At low coagulant doses, pC* had a linear relationship with the logarithm of PACl dose, indicating that turbidity and coagulant dose followed a power law relationship (Fig. 11). However, it was difficult to conclude which regression better fit the data in Fig. 14 because both the r squared values shown in Table 3 are quite high. Further studies over a wider range of coagulant doses should be conducted to see how floc number concentration is reduced as a function of coagulant dose.

Comparison between flocculated water and settled water

In Fig. 15, floc size distributions are compared between flocculated water and settled water to evaluate the performance of the tube settler. Flocculated water was sampled after the flocculator, while settled water was sampled after the tube settler.

Results confirm that sedimentation does little to remove particles below the capture velocity of the sedimentation tank. One concern with the results shown in Fig. 15 is that the concentration of small flocs (less than 5 μm) in the settled water was higher than that in the flocculated water. The inner diameter of the connecting tube between the tube settler and the turbidity meter was constrained by the 0.95 cm exit port diameter of the tube settler, thus the velocity gradient inside the connecting tube was 87/s, 24% higher than that inside the flocculator. The higher shear inside the connecting tube may break big flocs into small ones. However, preferential production of floc fragments smaller than 5 μm would not be expected. Another explanation for the observed increase in small flocs might be overlapping of flocs in the depth of field within the image volume. When there is a large floc in the image, small flocs behind or in front would not be detected by image analysis. The flocculated water has more large flocs (diameter greater than 70 μm) than the settled water. Therefore, the number of small flocs in flocculated water is more likely to be underestimated due to the image occlusion caused by big flocs. The number concentration of flocs for each bin size could possibly be corrected for occlusion by larger flocs to improve this analysis. The occluded volume would be obtained by the area of the larger flocs multiplied by the calculated depth of field.

Conclusions

This article presents an effective way to employ digital image analysis to continuously count and size flocs in a flow-through cell. Out-of-focus particles are automatically identified and excluded, thus improving the accuracy of the results of floc size measurement. The constraints for floc size measurements are the field of view, the depth of field, and the airy patterns caused by the objective lens. The apparatus could measure particle sizes ranging from around 2.6 μm to more than 300 μm. The error in measuring particle sizes caused by airy disk (light diffraction) was measured by testing particles of known diameter. The influence of airy disk accounted for a correction of 2.6 μm, which was consistent with the estimated diameter of the airy disk.

The average particle diameter of the test suspension of kaolinite clay was measured to be 7.7 ± 3.8 μm and a linear relationship was obtained between turbidity and the concentration of clay particles determined by imaging.

Size distribution of flocs could be plotted in varying bin sizes when the bin sizes increased with particle size following a power law. Since there are fewer large flocs, the bin size was kept proportional to the bin mean diameter to ensure that sufficient flocs were in the large bins to obtain a statistically meaningful particle count in each bin. Thus, varying the bin size with floc diameter can better reveal the shape of the size distribution curve. The shape and the area under the size distribution curves were independent of the bases used to set bin size.

For settled water, as was expected, floc number concentrations decreased when the PACl dose increased. pC* had a linear relationship with the logarithm of PACl dose. The maximum floc size observed in the effluent was less than 120 μm, which was in accordance with the value predicted by a model for the capture velocity of the experimental tube settler. Image occlusion caused by overlapping flocs may result in the underestimation of the number concentration of small flocs in flocculated water.

Image analysis of flocculated water could be used to predict particle counts after sedimentation. This has the potential to be used to improve performance of water treatment plants especially during raw water quality changes.

Acknowledgments

The authors thank the following staff at Cornell University who helped to make this research possible: Timothy Brock, Paul Charles, and Cameron Willkins. This research was funded, in part, by the National Science Foundation Award Number 1437961.

Author Disclosure Statement

No competing financial interests exist.

References

Adachi, Y., and Tanaka, Y. (1997). Settling velocity of an aluminum-kaolinite floc. *Water Res.* 31, 449.

Adelman, M.J., Hurst. M.W., Weber-Shirk, M.L., Cabrito, T.S., Somogyi, C., and Lion, L.W. (2013). Floc roll-up and its implications for the spacing of inclined settling devices. *Environ. Eng. Sci.* 30, 302.

Aroke, U.O., El-Nafaty, U.A., and Osha, O.A. (2013). Properties and characterization of kaolin clay from Alkaleri, northeastern Nigeria. *Int. J. Emerg. Technol. Adv. Eng.* 3, 387.

Boadway, J.D. (1978). Dynamics of growth and breakage of alum floc in presence of fluid shear. *J. Environ. Eng. ASCE* 104, 901.

Bouyer, D., Coufort, C., Line, A., and Do-Quang, Z. (2004). Experimental analysis of floc size distribution under different hydrodynamics in a mixing tank. *AIChE J.* 50, 2064.

Chakraborti, R.K., Atkinson, J.F., and Benschoten, J.E.V. (2000). Characterization of alum floc by image analysis. *Environ. Sci. Technol.* 34, 3969.

Coufort, C., Dumas, C., Bouyer, D., and Line, A. (2008). Analysis of floc size distribution in a mixing tank. *Chem. Eng. Process* 47, 287.

Edmund Optics. (2015). *Wavelength Effects on Performance*. Available at: www.edmundoptics.com/technical-resources-center/imaging/wavelength-effects-on-performance/ (accessed November 2015)

Gibbs, R.J. (1982). Floc breakage during HIAC light-blocking analysis. *Environ. Sci. Technol.* 16, 298.

Greivenkamp, J.E. (2004). *Field Guide to Geometrical Optics*. Bellingham, WA: SPIE Press.

Hopkins, D.C., and Ducoste, J.J. (2003). Characterizing flocculation under heterogeneous turbulence. *J. Colloid. Interface Sci.* 264, 184.

Jiang, Q., and Logan, B.E. (1991). Fractal dimensions of aggregates determined from steady-state size distributions. *Environ. Sci. Technol.* 25, 2031.

Keyvani, A., and Strom, K. (2013). A fully-automated image processing technique to improve measurement of suspended particles and flocs by removing out-of-focus objects. *Comput. Geosci.* 52, 189.

Klinger, T. (2003). *Image Processing with LabVIEW and IMAQ Vision*. Upper Saddle River, NJ: Pearson Education, Inc., pp. 162–171.

Li, D., and Ganczarczyk, J. (1989). Fractal geometry of particle aggregates generated in water and wastewater treatment processes. *Environ. Sci. Technol.* 23, 1385.

Matsuo, T., and Unno, H. (1981). Forces acting on floc and strength of floc. *J. Environ. Eng. ASCE* 107, 527.

Nan, J., He, W., Song, X., and Lu, G. (2009). Impact of dynamic distribution of floc particles on flocculation effect. *J. Environ. Sci.* 21, 1059.

National Instruments. (2008). *Image Analysis and Processing*. Available at: www.ni.com/white-paper/3470/en/#toc2 (accessed November 2015)

National Instruments. (2013). *Thresholding*. Available at: http://zone.ni.com/reference/en-XX/help/372916P-01/nivisionconcepts/thresholding/ (accessed November 2015)

Pal, G., and Pal, P. (2001). *Textbook of Practical Physiology*, 1st ed. Chennai, India: Orient Blackswan, p. 387.

Swetland, K.A., Weber-Shirk, M.L., and Lion, L.W. (2014). Flocculation-sedimentation performance model for laminar-flow hydraulic flocculation with polyaluminum chloride and aluminum sulfate coagulants. *J. Environ. Eng. ASCE* 140, 04014002.

Tambo, N., and Watanabe, Y. (1979). Physical characteristics of flocs-I. The floc density function and aluminum floc. *Water Res.* 13, 409.

Tse, I.C., Swetland, K., Weber-Shirk, M.L., and Lion, L.W. (2011). Method for quantitative analysis of flocculation performance. *Water Res.* 45, 3075.

Weber-Shirk, M.L. (2008). *An Automated Method for Testing Process Parameters*. Available at: https://confluence.cornell.edu/display/AGUACLARA/ProCoDA (accessed November 2015)

Wei, N., Zhang, Z., Liu, D., Wu, Y., Wang, J., and Wang, Q. (2015). Coagulation behavior of polyaluminum chloride: Effects of pH and coagulant dosage. *Chinese J. Chem. Eng.* 23, 1041.

Yao, M., Nan, J., and Chen, T. (2014). Effect of particle size distribution on turbidity under various water quality levels during flocculation processes. *Desalination* 354, 116.

Zhang, Z., Zhao, J., Xia, S., Liu, C., and Kang, X. (2007). Particle size distribution and removal by a chemical-biological flocculation process. *J. Environ. Sci.* 19, 559.